https://doi.org/10.5194/angeo-2022-18
Preprint. Discussion started: 5 September 2022

Annales Geophysicae Discussions

Latitudinal variations of ionospheric-thermospheric responses to Geomagnetic Storms from Multi-Instruments

Rasim Shahzad[a], Munawar Shah[a*], Ayesha Abbas[b], Amna Hafeez[a], Andres Calabia[c], Angela Melgarejo-Morales[d], Najam Abbas Naqvi[b]

[a] Department of Space Sciences, Space Education and GNSS Lab, National Center of GIS and Space Application, Institute of Space Technology, IST, Islamabad, 44000, Pakistan
[b] Department of Petroleum Engineering, NED University of Engineering and Technology, Karachi 75270, Pakistan
[c] School of Remote Sensing and Geomatics Engineering, Nanjing University Information Science Technology, China.
[d] Department of Earth and Space Science, Autonomous University of Sinaloa, Culiacan, Sinaloa, 80040, Mexico, Email:

[*]Corresponding author: munawar.shah@mail.ist.edu.pk

Abstract

Scintillations of transionospheric satellite signals during geomagnetic storms can severely threaten navigation accuracy and the integrity of space assets. We analyze vertical Total Electron Content (vTEC) variations from the Global Navigation Satellite System (GNSS) at different latitudes around the world during the geomagnetic storms of June 2015 and August 2018. The resulting ionospheric perturbations at the low-and mid-latitudes are investigated in terms of the prompt penetration electric field (PPEF), the equatorial electrojet (EEJ), and the magnetic H component from INTERMAGNET stations near the equator. East and South-East Asia, Russia, and Oceania exhibited positive vTEC disturbances, while South American stations showed negative vTEC disturbances during both storms. We also analyzed the vTEC from the Swarm satellites and found similar results to the GNSS retrieved vTEC during different phases of both geomagnetic storms. Moreover, we observed that ionospheric plasma tended to increase rapidly during the afternoon in

https://doi.org/10.5194/angeo-2022-18
Preprint. Discussion started: 5 September 2022

the main phase of the storms. At nighttime, the ionosphere depicted an opposite behavior under similar conditions. The equatorial ionization anomaly (EIA) crest expansion to mid and high latitudes is driven by PPEF during daytime at the main and recovery phases of the storms. The magnetic H component exhibits a longitudinal behavior along with the EEJ enhancement near the magnetic equator.

Keywords: Ionosphere, Geomagnetic Storms, Total Electron Content, Prompt Penetration Electric Field

1. Introduction

The Sun trigger space weather events such as geomagnetic storms that can cause negative impacts on communication and navigation through transionospheric electromagnetic signals on the Earth. Geomagnetic storms result from large-scale disturbances of the Earth's magnetosphere under variable solar activity, leading to anomalous ionosphere variability. These disturbances occur at short-term scales (hours to a few days) and are usually triggered by Coronal Mass Ejection (CME), Co-rotating Interaction Regions (CIRs), or fast-moving solar wind streams. Anomalous ionospheric variations are observed during geomagnetic storms from plasma content variability during the geomagnetic storms of 6 April and 29 May 2010 (Joshua et al., 2011; Adebiyi et al., 2012). Several studies have investigated the ionospheric variations during storms at different latitudes from satellite data (e.g., Fang et al. 2012; Adebesin et al. 2013; Calabia et al., 2022). Moreover, the seasonal variations and hemispherical ionospheric irregularities are also presented during geomagnetic storms (e.g., Tsurutani et al. 2004, Mannucci et al. 2005, Gao et al. 2008, Stankov et al. 2010). However, the overall perception of storm-time ionospheric variations across the different latitude ranges in both hemispheres is still uncertain.

Moreover, GNSS based TEC and in-situ data from multi-instruments describe the ionosphere abnormalities in different spatial and temporal resolution at different latitudes during solar and geomagnetic conditions (Chartier et al. 2018). The ionospheric irregularities have significant effects on GNSS signals in the low latitudes during main phase of the storm; however, the triggering reasons are unknown (Buchert et al. 2015; Xiong et al. 2016a). Transionospheric signal delay during storm conditions results in unacceptable GNSS positioning errors for practical

https://doi.org/10.5194/angeo-2022-18
Preprint. Discussion started: 5 September 2022

applications (e.g., Stankov et al. 2007, 2009; Warnant et al., 2007). Since the ionospheric delay in GNSS signal is not yet corrected, the Global Ionospheric Maps (GIMs) of TEC from the International GNSS Service (IGS) are an exceptional product to calibrate the ionospheric correction and eliminate discrepancies from GNSS signal with the help of other multi-instrument data.

Geomagnetic storms induce effects in the ionosphere at different latitudes and longitudes in the form of electric field penetration from high to low latitudes due to PPEF. Furthermore, the perturbations of global thermospheric circulation in high latitude induced joule-heating enhancement during geomagnetic activity leading to Disturbed Dynamo Electric Fields (DDEF). In the equatorial and low latitudes, the electrodynamics in the ionospheric E and F regions influences the plasma distribution (Heelis, 2004). Field Aligned Current System (FACS) controls the transfer of energy and momentum from the magnetosphere to the ionosphere in the form of two clear shells (Binod et al. 2017). These two shells include regions 1 and 2 for higher and lower latitudes connected through the ionosphere around the Earth, respectively. The neutral wind dynamo induced polarized electric fields in the low latitude during dayside (night side) in eastward (westward) direction (Fuller-Rowell, 2011). The horizontal component of magnetic field corresponds to zonal electric field generates electrons upwelling due to E×B effect. As a result, negatively and positively charged particles form on top and bottom of the ionospheric E region, respectively. At an altitude of 90-130 km, the migration of electrons produces an electric current known as the equatorial electrojet (EEJ).

Sharma et al. (2011) presented two enhanced peaks in TEC with twice in intensity as compared to quiet days in low latitude region as storm-time responses of August 25, 2005. They showed that the first peak in ionospheric TEC is due to PPEF and the second peak occurred due to plasma fountain. Moreover, the PPEF influences along the longitudes showed nearly homogeneous effects in the storm of August 25, 2005. On the other hand, the southward shifted interplanetary magnetic field (IMF) Bz component induced the increased activity in the high-latitude convection. Previous researches have provided insights on mid-latitude TEC enhancements during the initial phase of geomagnetic storms as compared to main phase (Hargreaves, 1992; Araujo-Pradere et al. 2006). For example, Astafyeva et al. (2016) showed the equatorial-and mid-latitudinal ionospheric TEC during main phase of the storm at different part of the world from multi-instrument satellite data.

https://doi.org/10.5194/angeo-2022-18
Preprint. Discussion started: 5 September 2022

Similarly, Astafyeva et al. (2017) also assessed the effects of the June 2015 geomagnetic storm with a comprehensive study using multiple satellite observations. They further demonstrated that the storm had major effects on the ionosphere due to thermospheric winds in the low-and mid-latitude regions. They also showed that dayside neutral mass density enhancement during storms exceeded the quiet period in the thermosphere due to strong and robust PPEF influences the ionosphere with significant variability. Moreover, Adebiyi et al. (2012) and Joshua et al. (2011) reported an enhanced electron density in the African equatorial region during the geomagnetic storms of 6 April and 29 May 2010.

Apart from above reports, positive and negative ionospheric anomalies due to geomagnetic storms can significantly vary depending on the duration of the solar activity, season, latitude, local solar time, etc., and each storm showed different characteristics. Clearly, we need to observe satellites with multiple instruments in order to find the missing drivers (Araujo-Pradere et al. 2006; Mannucci et al. 2008). This study comprises the understanding of the probable latitudinal mechanisms that influence the variable ionosphere by studying the geomagnetic storms of June 2015 and August 2018 using multi-instrumental data. In the following section, we present a brief description of the data and methods used in this study. Section 3 describes deeply the results, and section 4 discuss the observed magnetosphere-thermosphere-ionosphere (MIT) coupling during the storm. The last section summarizes the conclusions.

2. Data and Methods

In this paper, we study ionospheric response to the geomagnetic storms of 2015 and 2018 on global scale to find out the source triggered the ionospheric variations. In particular, we analyze the 3-hourly geomagnetic Kp index, the 1-min averaged electric Ey field, the IMF Bz component, the solar wind velocity Vsw, the aurora AE index, the geomagnetic disturbance storm time index (Dst), and the solar flux F10.7 index. The data is available at the Omni Web of NASA at http://omniweb.gsfc.nasa.gov/. The beginning of a geomagnetic storm usually exhibits a prompt decrease in the Dst index. The AE index can be used to study the energy transmitted to the auroral ionosphere during the storm. The Kp index can provide a good description of the magnitude of the storm; the range of Kp is between 0 to 9. The PPEF data is obtained from the real-time model of the Cooperative Institute for Research in Environmental Sciences website https://geomag.colorado.edu/real-time-model-of-the-ionospheric-electric-fields.html.

https://doi.org/10.5194/angeo-2022-18
Preprint. Discussion started: 5 September 2022

Annales Geophysicae Discussions

The Global Ultraviolet Imager (GUVI) onboard the Thermosphere-Ionosphere-Mesosphere Energetics and Dynamics (TIMED) satellite senses far-ultraviolet emissions and provides thermospheric [O/N2] ratio maps (Christensen et al., 2003). These maps are obtained from https://guvitimed.jhuapl.edu/. The [O/N_2] ratio is a measure of the electron density at the ionospheric F region; increases in N_2 decreases electron density (Prölss and Bird, 2010).

The TEC data from 15 different GNSS stations at low-mid and high-latitude regions were retrieved from the IONOLAB website, https://www.ionolab.org/. Fig. 1 shows the location of the GNSS stations used in this study and Table 1 details them. Slant TEC (STEC) is estimated as the number of free electrons in a square meter section along the line of sight between a GNSS satellite and receiver. The STEC units are TEC Units (TECU), where 1 TECU = 10^{16} electron/m^2. The STEC is obtained from IONOLAB and is processed by below equations (Arikan et al. 2008).

$$\mathrm{STEC} = \frac{f_1^2 f_2^2}{40.28(f_1^2-f_2^2)}\left(L_1 - L_2 + \lambda_1(N_1 + b_1) - \lambda_2(N_2 + b_2) + \epsilon\right) \quad (1)$$

$$\mathrm{STEC} = \frac{f_1^2 f_2^2}{40.28(f_1^2-f_2^2)}\left(P_1 - P_2 - (d_1 - d_2) + \epsilon\right) \quad (2)$$

In this equation, carrier phase frequencies are presented by f_1 and f_2, pseudo-range is denoted as L, the delay path of the signal of carrier phase observations is P, the signal wavelength is λ, and the ray path uncertainty is N. Here, d and b denote the biases of consequent signal pseudo-range and instrumental carrier phase, and ϵ is the random error in the signal. The STEC is converted to VTEC using the following equation (Shah et al. 2020):

$$\mathrm{VTEC} = \mathrm{STEC} \times \cos\left(arcsine\left(\frac{R\sin Z}{R+H}\right)\right) \quad (3)$$

In this equation, Z is the elevation angle of the satellite, and R and H are the Earth's radius and the ionosphere height, respectively (Klobuchar 1987).

Table 1. The details of GNSS stations used to study ionospheric variations.

https://doi.org/10.5194/angeo-2022-18
Preprint. Discussion started: 5 September 2022

	Region	Station	Receiver	Geographic Latitude (Longitude)	Geomagnetic Latitude (Longitude) 2015	Geomagnetic Latitude (Longitude) 2018
Low Latitude	South East Asia	Australia (COCO)	SEPT POLARX5	12.188°S (96.834°E)	21.62°S (168.89°E)	21.46°S (168.95°E)
		Indonesia (BAKO)	LEICA GR50	6.49°S (106.85°E)	16.13° S (179.44°E)	15.97°S (179.49°E)
		India (HYDE)	LEICA GRX1200G GPRO	17.417°N (78.551°E)	8.77°N (152.23°E)	8.92°N (152.26°E)
	South Asia	India (IISC)	SEPT POLARX5	13.021°N (77.570°E)	4.50° N (150.92°E)	4.64°N (150.9°E)
	Oceania	New Caledonia (KOUC)	TRIMBLE NETR9	20.559°S (164.287°E)	25.48°S (119.59°W)	25.40°S (119.61°W)
	South America	Ecuador (GLPS)	JAVAD TRE_G3TH	0.743°S (90.304°W)	8.49°N (17.89°W)	8.33°N (17.84°W)
		French Guiana (KOUR)	SEPT POLARX5 TR	5.252°N (52.640°W)	14.31°N (20.55°E)	14.15° (20.58°E)
		Ecuador (RIOP)	TRIMBLE NETRS	1.651°S (78.651°W)	7.99N (6.09W)	7.83°N (6.05°W)
Mid Latitude	Oceania	New Zealand (AUCK)	TRIMBLE ALLOY	36.6.3°S (174.834°E)	39.58°S (105.37°W)	39.53°S (105.47°W)
	East Asia	Japan (STK2)	TRIMBLE ALLOY	43.529°N (141.845°E)	35.14°N (149.78°W)	35.29°N (149.69°W)
		Japan (USUD)	SEPT POLARX5	36.133°N (138.362°E)	27.51°N (151.98°W)	27.66°N (151.91°W)
	Eastern Europe and Russia	Russia (YSSK)	JAVAD TRE_3N	47.030°N (142.717°E)	38.69°N (149.55°W)	38.84°N (149.45°W)
	South America	Chile (SANT)	SEPT POLARX5	-33.150°S (70.669°W)	-23.29°S (1.78°E)	-23.46°S (1.81°E)
High Latitude	Western Europe	Sweden (KIR0)	SEPT POLARX5	67.878°N (21.060°E)	65.26°N (115.42°E)	65.33°N (115.13°E)
		Sweden (MAR6)	SEPT POLARX5	60.595°N (17.259°E)	59.04°N (106.40°E)	59.08°N (106.17°E)

Moreover, we also study the ionospheric indices from Swarm satellites to provide more evidence to vTEC variations from GNSS. The Swarm mission is comprised of three identical satellites, where Swarm A and C orbit at 440-460 km height and Swarm B track is at 520-530 km height. These satellites carry sophisticated magnetometers, an Electric Field instrument to measure electron density (Ne), and a GNSS receiver to provide vTEC. Moreover, all satellites have polar orbits with inclination angle of 87°- 88°. The vTEC data from Swarm is available at https://vires.services. The Swarm data was also analyzed during the different phases of both the storms.

https://doi.org/10.5194/angeo-2022-18
Preprint. Discussion started: 5 September 2022

Annales Geophysicae Discussions

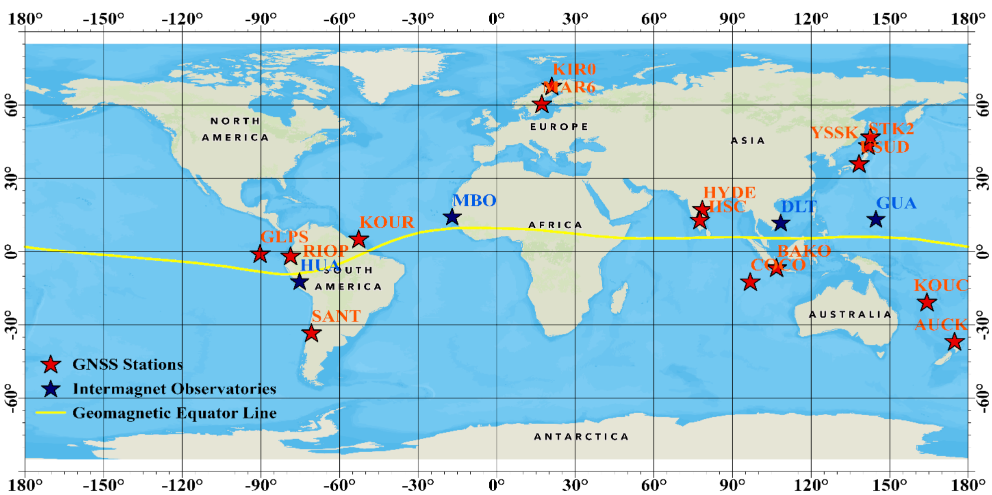

Fig. 1. Geographic location of GNSS and INTERMAGNET stations used in this study. The yellow line represents the magnetic equator. The corresponding coordinates are given in Table 1.

Furthermore, vTEC and dTEC from GNSS of IGS network is analyzed in bi-hourly temporal resolution and spatial resolution of 2.5° by 5° in latitude and longitude, respectively (Hernández-Pajares et al. 1999; Roma-Dollase et al., 2018). The maps are available in the IONEX (IONosphere map Exchange) format at the Crustal Dynamics Data Information System (CDDIS) Goddard Space Flight Center (GSFC) National Aeronautics and Space Administration (NASA) website https://cddis.nasa.gov/index.html.

In order to investigate the abrupt TEC anomalies during geomagnetic storms, the new empirical vTEC model of Calabia and Jin (2020, 2019) is used as quiet-time background. In this model, vTEC observables from 2003 to 2018 were reduced to a lower-dimensional through the principal component analysis, and the resulting time-expansion coefficients were parameterized in terms of solar and magnetospheric forcing, annual, and LST cycles. The quiet magnetospheric forcing is set during the geomagnetic index condition at Am=6. In this scheme, the diurnal, annual, and solar cycle variations are eliminated, and the residuals mainly show the short-term variations due to magnetospheric forcing; i.e., those variations mainly caused due to geomagnetic storms. The Calabia and Jin model is available at https://zenodo.org/record/3563463.

The Earth's magnetic field components are obtained from the magnetometer stations near the magnetic equator. This data aims to help investigate the E region response during various phases of the geomagnetic storms. The data at 1-min resolution is available at the INTERMAGNET network http://intermagnet.org. We employ data from the stations at HUA (America), GUA (Pacific Ocean), and MBO (Africa). The geographic and geomagnetic coordinates of the magnetometer stations are listed in Table 2, and their locations are shown in Figure 1. According to Biot and Savart's law, ground magnetic field perturbations can be an integral part of ionospheric and magnetospheric electric current (Shao et al., 2002; Le and Amoray-Mazaudier, 2005). The horizontal component (H) of geomagnetic field can be computed using the north (X) and east (Y) components of the magnetic field (i.e., $H = \sqrt{X^2 + Y^2}$). The observed H component corresponds to the current flow into the magnetosphere-ionosphere systems (Cole, 1966). The equation is as follows:

$$H = S_R + D \quad (4)$$

In this equation, S_R and D represent the solar regular variations of Earth's magnetic field due to regular ionospheric dynamo and the combined effect of various current systems flowing in the MI system, respectively (Zaourar et al., 2017). According to Le and Amoray-Mazaudier (2005), the H component can be rewritten as follows:

$$H = H_0 + S_R + D_M + D_{iono} \quad (5)$$

In this equation, H_0 and S_R are Earth's core induced baseline magnetic field and regular variation of Earth's magnetic field on a given day, respectively. Whereas, magnetic field variations associated to magnetosphere and ionosphere currents are represented as D_M and D_{iono}, respectively. The D_{iono} is estimated as follows (Le and Amoray-Mazaudier, 2005):

$$D_{iono} = H - D_M - S_q \quad (6a)$$

$$D_{iono} = DP2 + D_{dyn} \quad (6b)$$

In this equation, D_{iono} consists on the combined effect caused by ionospheric disturbance due to polar currents (DP2) and dynamo currents (D_{dyn}) at low latitudes, DP2 is associated with PPEF, and D_{dyn} is associated with DDEF (Nishida, 1968; Le and Amoray-Mazaudier, 2005). D_M is calculated using the SYM-H index and the dip angle Φ as follows:

$$D_M = SYM\text{-}H * \cos(\Phi) \quad (7)$$

https://doi.org/10.5194/angeo-2022-18
Preprint. Discussion started: 5 September 2022

Annales Geophysicae
Discussions
Open Access

In equation 6a, S_q represents the average of selective quiet days (S_R). Here, 5 quiet days are considered to compute S_q. We average the H component as suggested by the German Research Center of Geosciences (GFZ) (ftp://ftp.gfz-potsdam.de/pub/home/obs/kp-ap/quietdst/). The results are shown in Table 3, and the equation of S_q is as follows:

$$S_q = \langle H^{quiet} \rangle = \frac{1}{n}\sum_{i=1}^{n} H_i^{quiet} \qquad (8)$$

The EEJ at each station is computed by differences of the H component inside and outside the EEJ region at similar longitudes. These differences are related to the contribution of the EEJ current (Anderson et al., 2004):

$$EEJ = H_1 - H_2 \qquad (9)$$

In equation 9, H_1 and H_2 are the average of H components inside and outside the EEJ region, respectively.

https://doi.org/10.5194/angeo-2022-18
Preprint. Discussion started: 5 September 2022

Table 2. The geographic and geomagnetic locations and magnetic dip angle of Magnetometer stations.

Region	*Station Code*	*Geographic Latitude (Longitude)*	*Geomagnetic Latitude (Longitude)*		*Dip Angle*	
			2015	*2018*	*2015*	*2018*
America	***HUA***	12.0686°S	2.31°S	2.48°S	-0.3612°	-0.8384°
		(75.2103°W)	(2.54°W)	(2.50°W)		
Pacific Ocean	***GUA***	13.4443°N	5.61°N	5.74°N	12.4583°	12.3219°
		(144.7937°E)	(143.57°W)	(143.52°W)		
Africa	***MBO***	14.4228°N	19.63°N	19.54°N	7.0608°	6.6283°
		(16.9654°W)	(58.13°E)	(58.12°E)		
Asia	***DLT***	11.9404°N	2.18°N	2.34°N	11.230°	11.6661°
		(108.4583°E)	(178.95°W)	(178.91°W)		

Table 3. The selected magnetic quiet day to calculate Sq during June 2015 and August 2018 storms.

	Q1	**Q2**	**Q3**	**Q4**	**Q5**
June, 2015	20	5	2	4	3
August, 2018	6	14	10	13	23

3. Results

3.1 The Geomagnetic Storms of June 2015 and August 2018

The geomagnetic storm of June 2015 occurred during the solar cycle 24, and it was the second largest known storm after the St. Patrick's storm. On 22 June 2015, two CMEs hit the Earth's magnetosphere at 05:45 UT and 18:35 UT. Figures 2-3 shows the Sudden Storm Commencement (SSC), where the different phases are classified on the basis of different storm indices. The IMF Bz component shows a sharp southward turning immediately after the SSC, followed by a second

https://doi.org/10.5194/angeo-2022-18
Preprint. Discussion started: 5 September 2022

southward IMF Bz before the main phase. These IMF Bz turnings are associated with more than 720 km/s speed of solar wind after the second SSC.

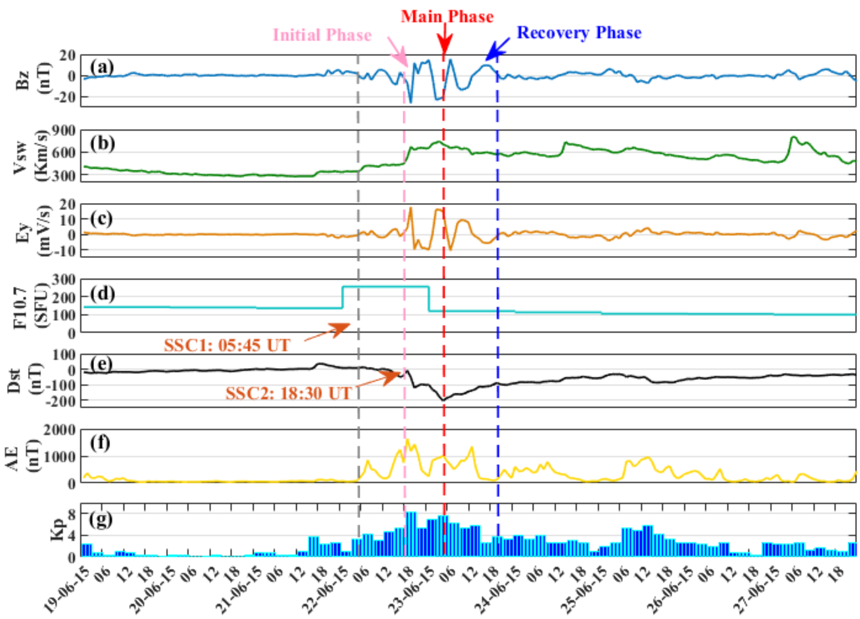

Fig. 2. Space weather indices for the storm of 22 June 2015. The SSCs are marked with red arrows and different phases of the storm are marked with vertical dashed lines.

The storm of August 2018 occurred due to a large CME ejection from the Sun on 20 August 2018 (Figure 3). Formerly, scientist from the National Oceanic Atmospheric Administration (NOAA) called it a minor storm due slow speed stream but later on a G4 severe geomagnetic storm evolved as long term southward IMF Bz; i.e., from 15:55 h UT on 25 August to 09:45 h UT on 26 August, thus allowing a large number of particles entering the Earth's magnetosphere. The SSC initiated at 09:00 UT on 25August 2018 and, after 3 hours of the SSC, at 09:00 h UT, a rapid drop in Dst index was observed until 23:00 h UT on 23 August. The lowest Dst value was -203nT around 07:00 h UT on 26 August.

https://doi.org/10.5194/angeo-2022-18
Preprint. Discussion started: 5 September 2022

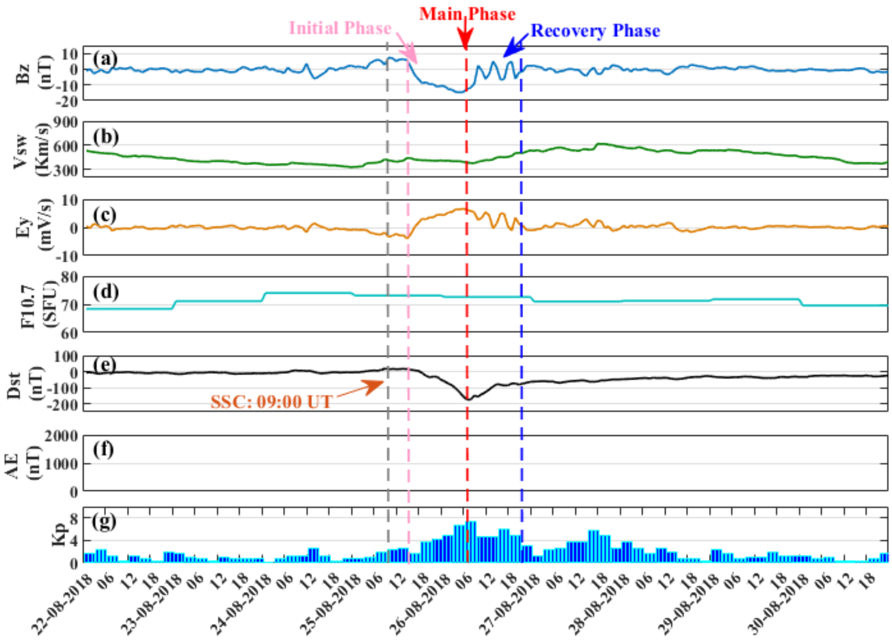

Fig. 3. Space weather indices during the storm of 26 August 2018 from OMNI web NASA. The SSC is marked with a red arrow and the different phases of the storm are marked with different color vertical dashed lines.

3.2 Ionospheric-Thermospheric Irregularities

The vTEC variations occurred at low-latitude stations in South America, South Asia, South East Asia, and Oceania region effect during the 2 geomagnetic storms (Figure 4). During the initial phases of both the storms, no clear enhancements occurred at the low latitude GNSS stations. However, for both storms, the GNSS stations at South East Asia showed significant vTEC variations during the main phase. For the South American stations, only the KOUR showed significant variability. Although both storms are of similar intensity, VTEC enhancements of > 50 TECU, 42<TECU<50, and 40< TECU<45 occurred in the low latitude stations of South East Asia, South Asia and American stations, respectively, during main phase of June 2015 storm. On the other hand, vTEC variations occurred in the range of 18 <TECU<20, 42<TECU<50, 40< TECU<45, and 18 <TECU<20 for COCO, BAKO, South Asia, and KOUR GNSS stations in 2018 during the main phase of the storm, respectively. Moreover, there were not significant variations in vTEC during the recovery phases of 2015 and 2018 storms; only a minor depletion in the South

https://doi.org/10.5194/angeo-2022-18
Preprint. Discussion started: 5 September 2022

American stations. During the recovery phase, TEC depletions in South American stations were more prominent in 2015 than in 2018.

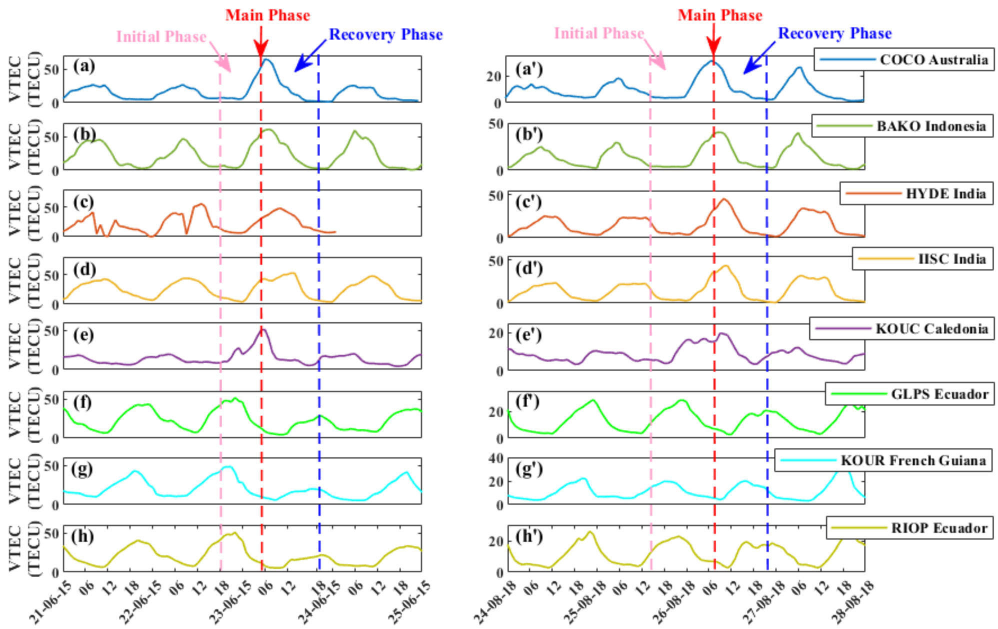

Fig. 4. vTEC variation at the low-latitude stations in different longitudinal sectors for the geomagnetic storms of 2015 and 2018. The locations of the stations are showed in Figure 1. The different phases of the storm are marked with vertical dashed lines.

The vTEC variations at the mid-latitude GNSS stations are shown in Figure 5. We employ the AUCK station in New Zealand, the STK2 and USSD stations in East Asia, the YSSK station in Russian, and the SANT station in Chile. During the initial phases of both storms, no clear vTEC variations occurred in any of the stations; only the SANT station showed a weak variation. During the main phases of both storms, the sharp enhancements are shown for all stations; except for the SANT station. The vTEC during the main phase of the 2015 geomagnetic storm at Oceania, East Asia, and Russia is 30<TECU<40, 30<TECU<40, 20<TECU<30, respectively. On the other hand, Oceania, East Asia, and Russia exhibited 10<TECU<20, 10<TECU<20, 10<TECU<20 during the 2018 geomagnetic storm, respectively. All the mid-latitude stations showed no significant anomalies during the recovery phases of both storms.

https://doi.org/10.5194/angeo-2022-18
Preprint. Discussion started: 5 September 2022

Annales Geophysicae Discussions
Open Access
EGU

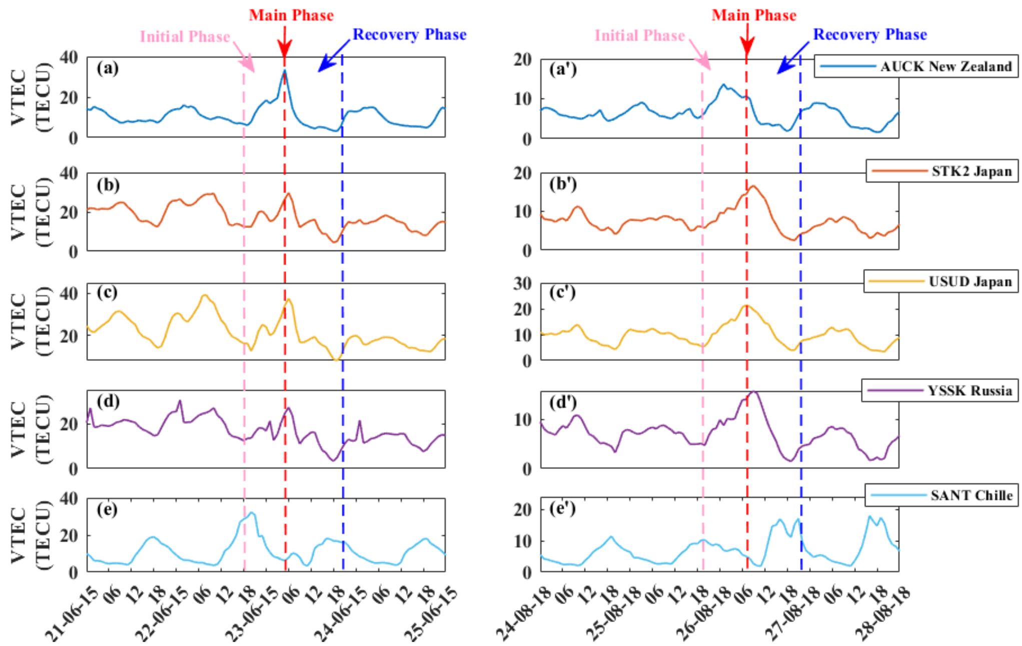

Fig. 5. vTEC variation at the mid-latitude stations in different longitudinal sectors for the geomagnetic storms of 2015 and 2018. The locations of the stations are showed in Figure 1. The different phases of the storm are marked with vertical dashed lines.

The vTEC at the high-latitude stations of KIR0 and MAR6 in Sweden and Europe are shown in Figure 6. In this Figure, enhancements of 2 TECU in KIR0 are shown within 2 hours after the SSC of the storm of 2015; Then, a sudden depletion until the main phase of the storm occurred. Similarly, the MAR6 station increases 4 TECU after the SSC, and then a depletion in the main phase occurred. In the recovery phase, no increases were seen for both stations.

https://doi.org/10.5194/angeo-2022-18
Preprint. Discussion started: 5 September 2022

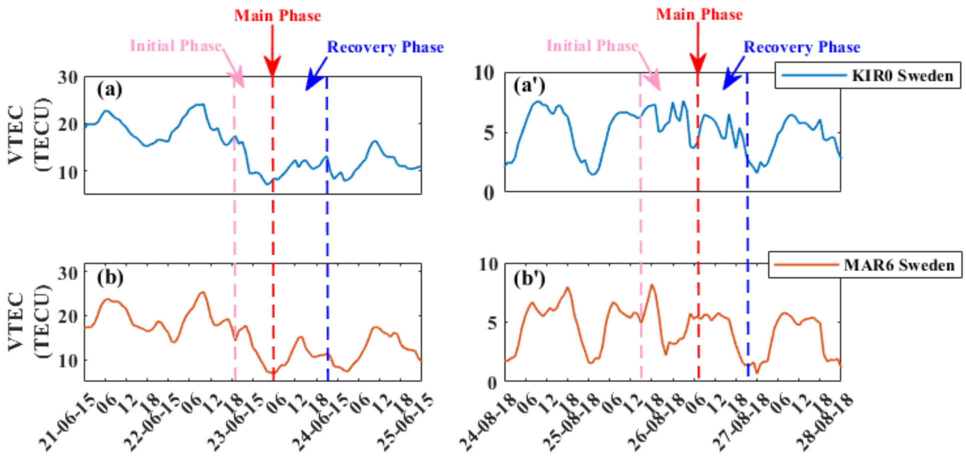

Fig. 6. vTEC variation at the high-latitude stations in different longitudinal sectors for the geomagnetic storms of 2015 and 2018. The location of the stations is shown in Figure 1. The different phases of the storm are marked with vertical dashed lines.

The TEC variations in GIMs for both storms are shown in Figures 7-8. During the storm of 2015, all 3 American, African, and Asian sectors showed a moderate high-latitude enhancement after the SCC at the southern latitudes. Then, the American and African sectors showed strong enhancements at the low-latitude regions above 15 dTECU, whereas the Asian sector showed depletion of similar magnitude. For this storm, the high-latitude regions showed a clear depletion during the main phase for all the 3 longitudes. During the main phase of the 2018 storm, vTEC enhancements were very prominent in the American and African sectors, in comparison to that in the Asian sector. As compared to the storm of 2015, no clear depletions were seen at any location.

https://doi.org/10.5194/angeo-2022-18
Preprint. Discussion started: 5 September 2022

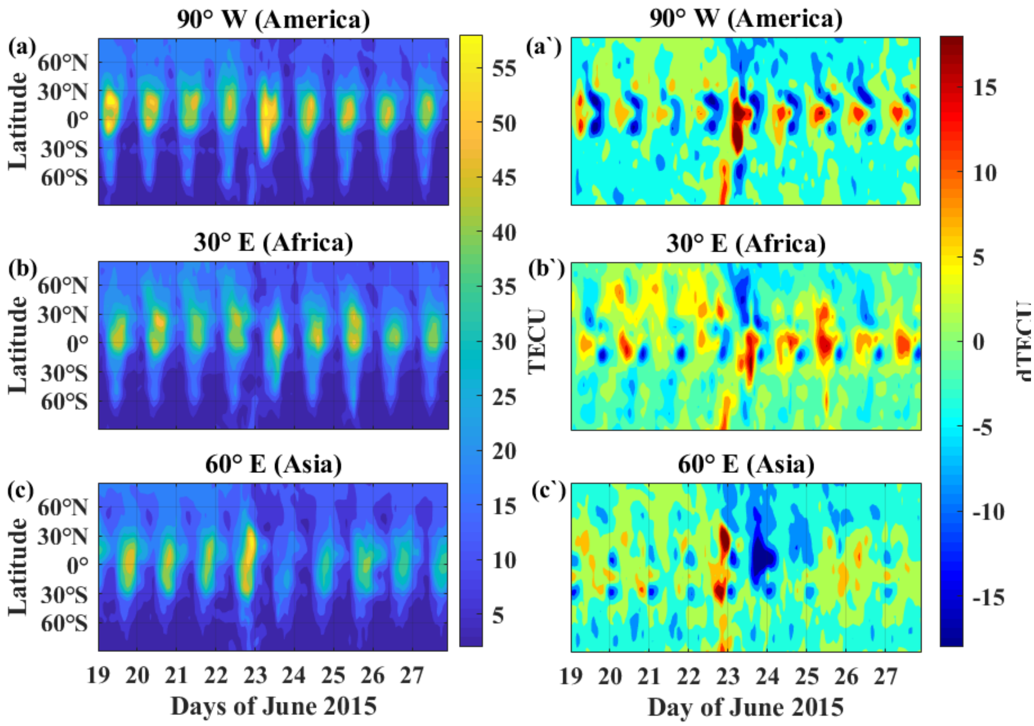

Fig. 7. GIM TEC maps at different longitudinal sectors during the June 2015 geomagnetic storm where; a-c) are TEC maps of America, Africa and Asia region, and a`-c`) are dTEC maps of America, Africa and Asia.

https://doi.org/10.5194/angeo-2022-18
Preprint. Discussion started: 5 September 2022

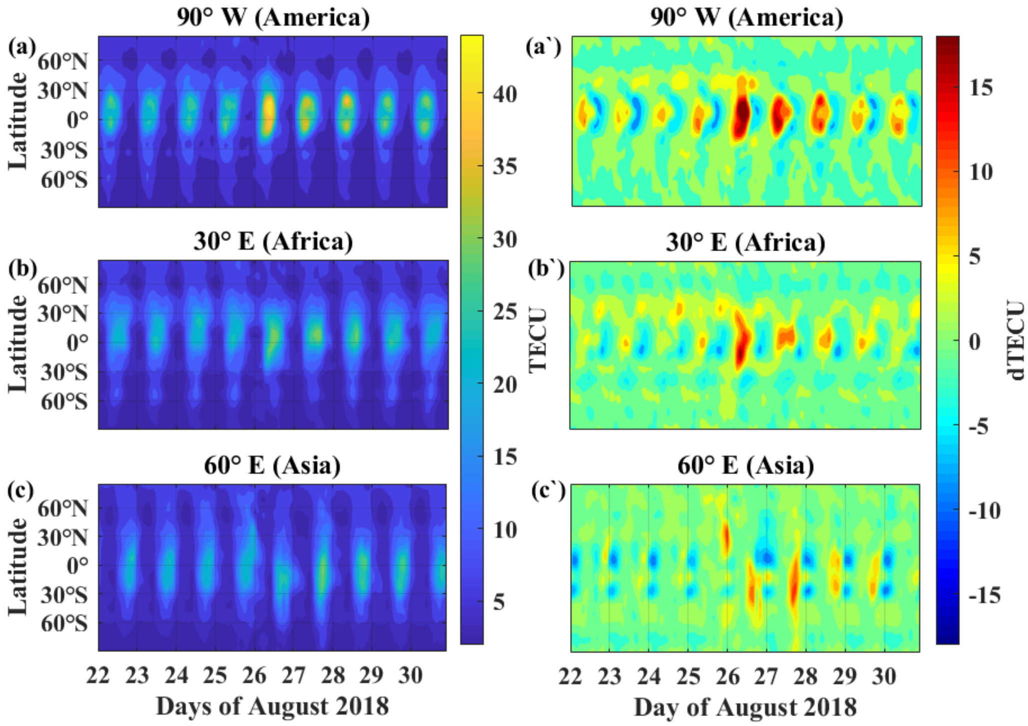

Fig. 8. GIM TEC maps response to geomagnetic storm of August 2018 where a-a`) TEC and dTEC maps of America, b-b`) TEC and dTEC map of Africa and c-c`) TEC and dTEC map of Asia region

Figure 9 shows the O/N2 ratio during the storms of 2015 and 2018. The African sector showed reductions of O/N2 ratio in the low-and mid-latitudes during the main phase of the 2015 storm. This resulted in the increment of vTEC in the African region. The Asian, Australia, and Oceania regions also showed significant enhancements in O/N2 ratio during the main phase of the 2015 geomagnetic storm and it result in vTEC depletion in the above mentioned regions. On the other hand, we also observe enhancement in O/N2 ratio (depletions in vTEC) in South American and Asian regions during the main phase of the 2018 geomagnetic storm. There are several reports in enhancement/depletion in O/N2 ratio (reduction/enrichment in vTEC) in different part of the world through thermospheric O/N2 variability (Martinis et al. 2005; Buresova et al. 2014; Kassa & Damite, 2017).

https://doi.org/10.5194/angeo-2022-18
Preprint. Discussion started: 5 September 2022

Annales Geophysicae Discussions

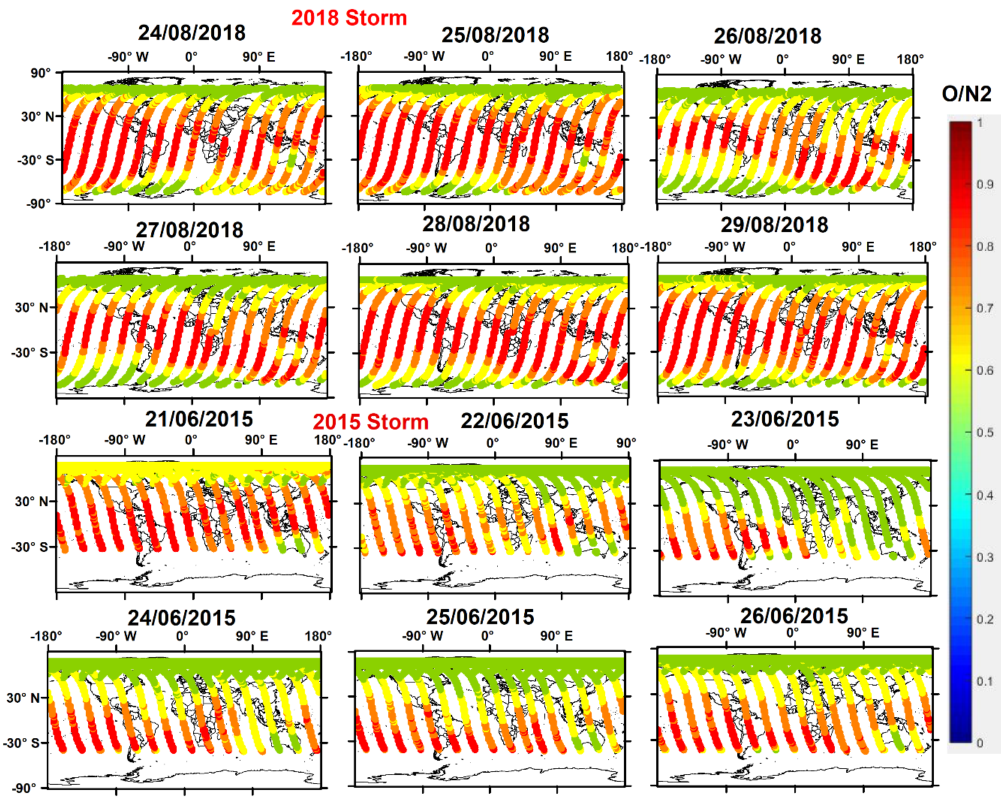

Fig. 9. The O/N2 ratio from GUVI during the storms of June 2018 and August 2015.

The vTEC from Swarm satellites for both the storms is shown in Figures 10-11. Clear enhancements were seen in the American region at the low-and mid-latitudes during the initial phase of both storms; no clear variations were observed for the Asian region during the initial phase of both storms. The low-and mid-latitudes of the Asian and African regions depicted larger VTEC variations than those in the American sector during the main phase of both storms. During the recovery phase of both storms, larger variations were observed at the American region than those at the Asian sector. The VTEC values from Swarm during the main and recovery phases were different than those from the GNSS stations in Asia, Australia and Russia.

https://doi.org/10.5194/angeo-2022-18
Preprint. Discussion started: 5 September 2022

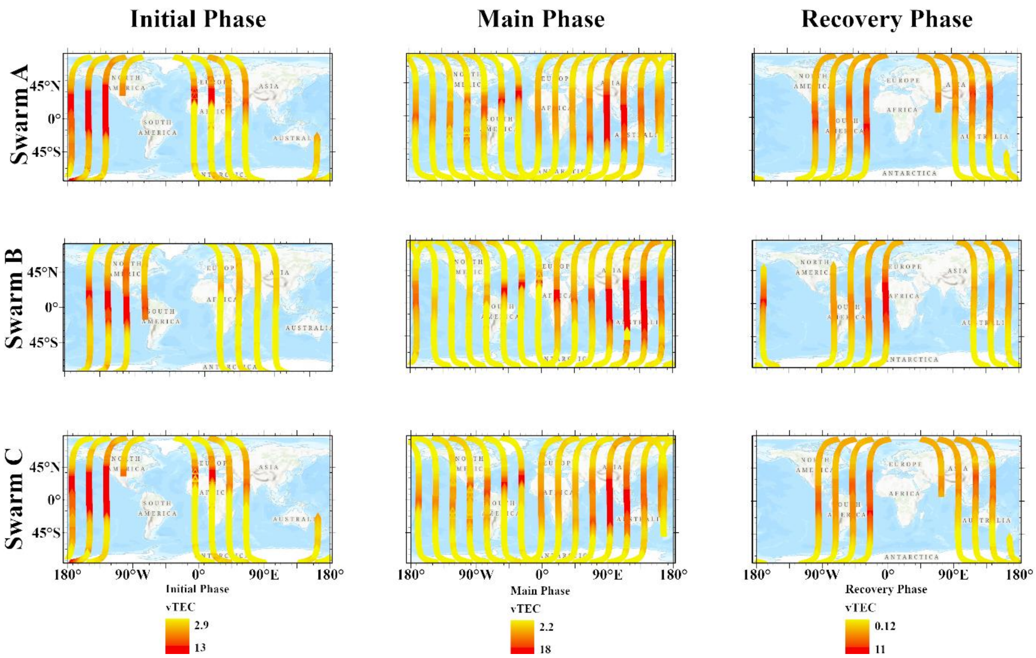

Fig. 10. The VTEC from Swarm during the geomagnetic storm of June 2015.

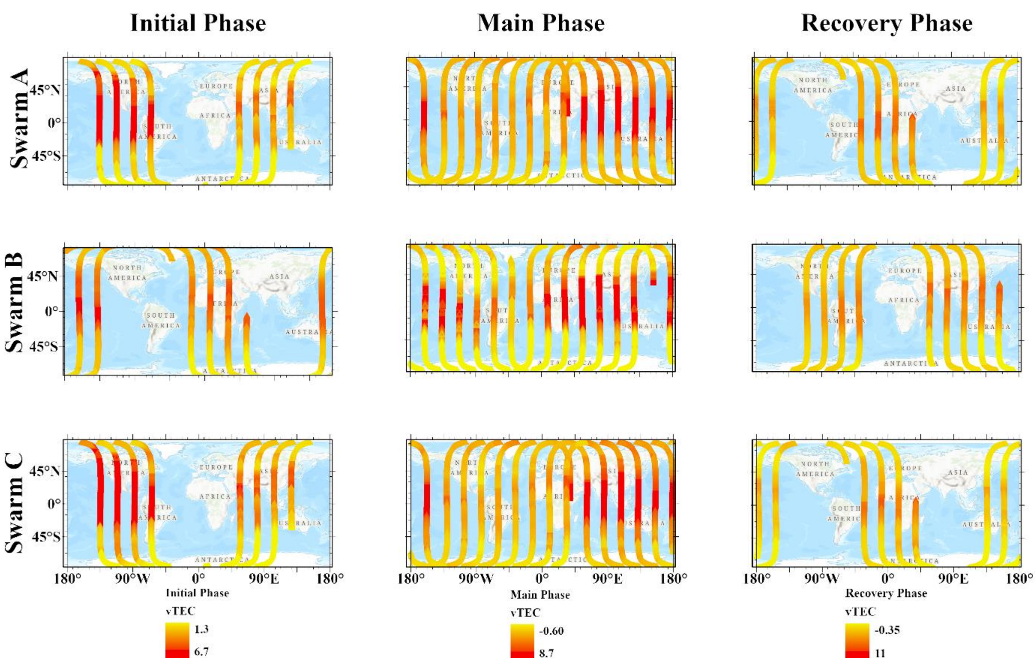

Fig. 11. The VTEC from Swarm during the geomagnetic storm of August 2018.

https://doi.org/10.5194/angeo-2022-18
Preprint. Discussion started: 5 September 2022

Annales Geophysicae Discussions
Open Access
EGU

The PPEF variations at the low-and mid-latitude regions during both storms are shown in Figure 12. The PPEF variations during the 2018 storm were smaller than those during the storm of 2015. This is different from the results obtained through IGS GIMs VTEC (Figures 7 and 8). Moreover, strong PPEF occurred at all longitudes during the main phase of the storm of 2015, while the PPEF peak during the 2018 storm occurred in the far East and West. During the main phase of both storms, stronger PPEF occurred in comparison to that seen during the other phases.

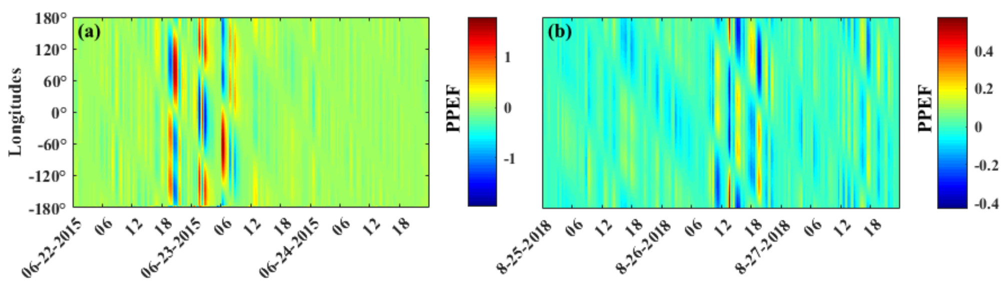

Fig. 12. PPEF behavior during geomagnetic storms where a) is June 2015 geomagnetic storm and b) is geomagnetic storm of August 2018.

3.3 Earth's Magnetic Field Variations

The variations in the Earth's magnetic field during the storms of June 2015 and August 2018 are shown in Figure 13. We investigate the variations in the H-component of Earth's magnetic field and the EEJ estimated from INTERMAGNET stations near the magnetic equator. This shows significant variations at the SSC events during both storms, followed by a considerable decrease in Earth horizontal component during the recovery phases. The largest disturbances of the H component in the American region (HUA station) reached 259.92 nT on 22 June 2015 at 20:49 h UT. Moreover, on 25 August 2018 at 23:55 h UT the initial phase of the storm reached -123.91 nT. The D_{ion} exhibited a decrease in the initial phase, followed by an increase in the main phase, this due to H minima during nighttime in the South American region. Two negative peaks in the H component were observed during the storm of June 2015 in the Pacific region, one during the beginning of the initial phase, and other during the main phase. Similarly, only one negative peak

https://doi.org/10.5194/angeo-2022-18
Preprint. Discussion started: 5 September 2022

Annales Geophysicae
Discussions
Open Access

was observed in the main phase during the storm of August 2018. The values of D_{ion} exhibited abrupt variations for both storms after each respective SSC, corresponding with the variations in the H component. The MBO station in Africa and the DLT station in Asia showed prominent decreases in the H component for both storms. The lowest values were -207.12 nT for the storm of June 2015 and -107.78 nT for the storm of August 2018. The VTEC variations triggered by D_{ion} were prominent at different longitudes, specifically during the SSC and the main phase of the storm of June 2015. No clear variations were seen in the HUA station during the storm of August 2018.

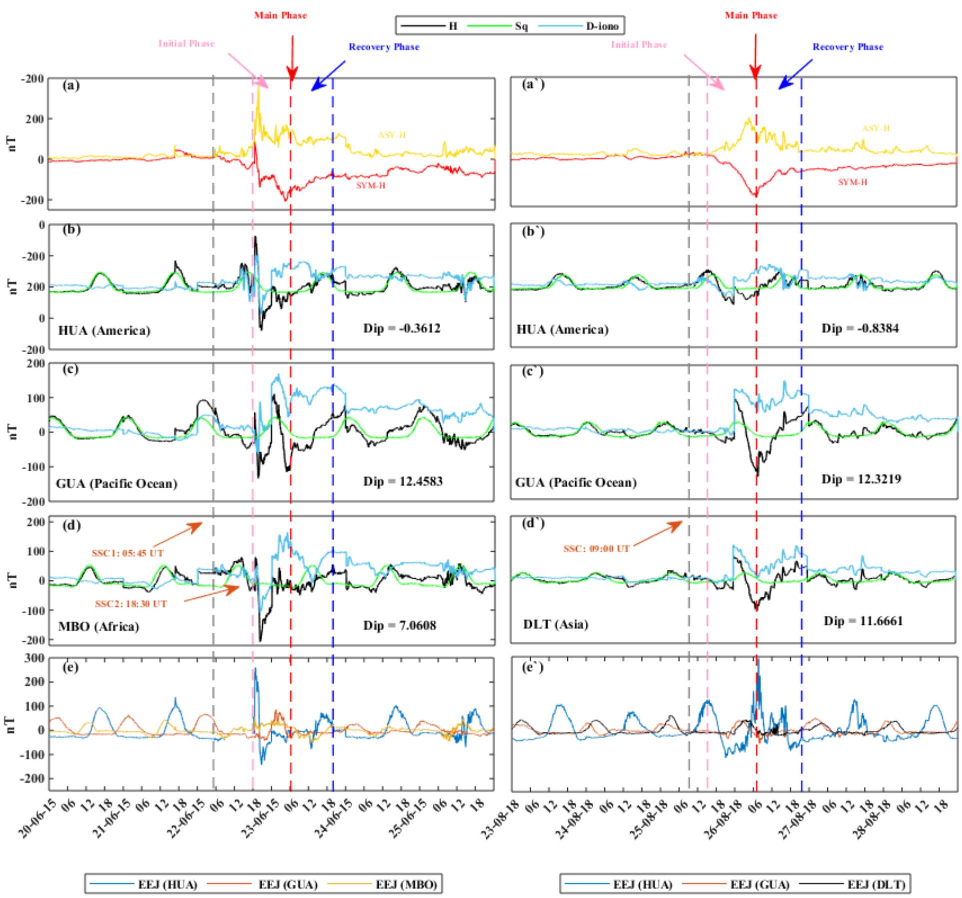

Fig. 13. Magnetic field variability during the storms of June 2015 and August 2018. a and a`) have the variation of SYM-H and ASY-H index, in (b-d) we show the H component in 2015 at HUA, GUA and MBO stations, in (b`-d`) we show the H component in 2018 at HUA, GUA and DLT

https://doi.org/10.5194/angeo-2022-18
Preprint. Discussion started: 5 September 2022

stations, and in (e & e`) we show the EEJ responses. The SSC is marked with a red arrow. The different phases of the storm are marked with vertical dashed lines.

4. Discussion

The VTEC enhancements during the storms of June 2015 and August 2018 initiated approximately 4 hours after the SSC events at the low-latitude regions in East Asia, South East Asia and Oceania. All the 3 sources of VTEC data used in this study, i.e. GNSS, Swarm, and IGS GIM TEC, have provided similar results with minor differences, specifically between GNSS and IGS GIM TEC, most likely due to local anomalies not well represented by GIM TEC (Lisa et al. 2020). All the VTEC enhancements occurred during the main phase for all 3 datasets. The variations at different geographical coordinates followed the PPEF and thermospheric O/N2 variations. Moreover, the PPEF enhancements started at the SCC in Asia and Oceania, along with the O/N2 enhancements leading to clear effects during the main phase at the low-latitude regions (Figs. 9 & 12). These positive enhancements are due to PPEF and the increment of oxygen (Klimenko et al. 2011). On the other side, no prominent enhancements or depletions occurred in the South American sector, most likely due to Dst minimum, along with depletion in the recovery phase due to a drop in O/N2 ratio (Figs. 4 & 9).

At the mid-latitudes, the Asia-Oceania region exhibited peak values during the main phase of the storms, coinciding with Dst minima. The station from South America exhibited depletions at the night side during the storm of June 2015; the storm of August 2018 lacked this feature. The EIA expansion from equatorial regions to mid-latitude regions was responsible for VTEC enhancements at all longitudes. Both storms analyzed here revealed that D_{ion} and O/N2 drivers control these fluctuations. In fact, Fuller-Rowell et al. (1994), Mannucci et al. (2005), and Vankadara et al. (2022) presented similar results. The PPEF plays a vital role in VTEC enhancements through plasma diffusion along magnetic field lines, thus creating the fountain effect during the daytime (Mannucci et al. 2005). The depletions seen in VTEC were due to variations in thermospheric composition such as those generated by recombination processes creating N_2. These depletions were observed in the recovery phase of both storms in the low-latitude South American regions (Figs. 4 & 9).

External electric field can penetrate into equator to disturb low and mid latitudes, as they are connected to inner magnetosphere through closed magnetic field lines. External sources should

https://doi.org/10.5194/angeo-2022-18
Preprint. Discussion started: 5 September 2022

Annales Geophysicae Discussions

also be considered, taking into account the fundamental forces that drive the penetration of electric field, such as solar wind drivers. Nishida (1968) compared the north-south oscillation in IMF with the geomagnetic fluctuations, and Jaggi and Wolf (1973) considered PPEF as a temporary failure mechanism of shielding. PPEF can exhibit multiple pulses, as it is the direct consequence of IEF fluctuations (Kelley et al. 1979). Magnetic reconnection is an important parameter for dusk-ward PPEF processes (lasting < 3h), and the dawn-ward IEF shows the opposite behavior, as long IMF Bz oscillates between northward and southward polarity; dawn-ward IEF rarely does. Wei et al. (2010) pointed out that the shielding effect would not fully develop under these circumstances, and would not cancel the PPEF during the short pulse of dusk-ward IEF. Nevertheless, this is not always the case since the transition to the northward IMF Bz component does not necessarily generate over-shielding. However, the reduction in the convective electric field can transit to over-shielding status (Wei et al. 2010). The magnetosphere under sustained pressure due to dense solar winds can suppress the development of electric field shielding during multiple PPEF events. PPEF can exhibit long-duration patterns as long as the magnetic activity is being strengthened under storm conditions (Huang et al. 2005). In this work, PPEF has demonstrated to generate variations in VTEC throughout the globe, except for the South America region, which was more prominent during the storm of June 2015. The max PPEF was confined to only the far East and West regions during the storm of August 2018, depicting clear variations in Oceania and not in the American sector. As the storm commenced, Asia, Oceania, and Russia exhibited VTEC enhancements at the low- and mid-latitudes due to PPEF. Storm time variations at the low- and mid-latitudes were generated by a large fountain effect, creating a stronger EIA. In fact, many researchers (Manucci et al. 2005; Abdu et al. 2007; Sharma et al. 2011; Lu et al. 2013) have reported these effects. The ionosphere exhibited a variable response along different longitudes. This has also been confirmed by different magnitudes of PPEF and satellite data (Figs. 4-8 & 10-12). Fagundes et al. (2016) demonstrated that the influence of PPEF in EIA shows significant longitudinal differences during geomagnetic storms.

During these geomagnetic storms, the Earth's magnetic field observations at different longitudes make possible to comprehend the processes of large-scale ionosphere electric currents. There are 2 main types of disturbances, namely DP2 and D_{dyn}, which are associated with PPEF and DDEF, respectively. D_{dyn} exhibits a more dynamic variation in comparison to DP2, which only lasts for 2 to 3 hours (Nishida et al., 1968; Le and Amory-Mazaudier (2005). During these geomagnetic

https://doi.org/10.5194/angeo-2022-18
Preprint. Discussion started: 5 September 2022

storms, normal circulation of thermospheric winds are perturbed due to moment transfer and energy inputs at high latitudes, giving eastward and westward electric field at the nightside and dayside, respectively (Blanc & Richmond, 1980; Fuller-Rowell et al. 2002). D_{iono} exhibited large nighttime enhancements at the low-latitude stations. These variations are associated with PRC, as indicated by ASYM-H (Fig. 13a & 13a`). The anti-Sq signatures observed during the recovery phase in the magnetic data are due to the orientation of electric fields (Yamazaki & Kosch 2015). Vankadara et al. (2022) did a similar study, where the authors showed D_{ion} minima at different Local Solar Time (LST) locations, leading to equatorial plasma bubble developments. Our results have shown differences in longitude because of magnetospheric convection processes and electric field penetration (Fejer et al. 2008). In this scheme, all three American regions have shown clear variations in the initial phases, but none in the main phases of both storms (Figs. 4 - 5, -7 - 8, and 10 - 11). On the other side, Asia, Oceania, and Russia have shown VTEC enhancements during the main phases (Figs. 4, 5, 7, 8, 10 & 11). Various authors have shown latitudinal and longitudinal ionosphere responses due to PPEF (Kikuchi et al. 2000; Mene et al. 2011; Kashcheyev et al. 2018). The EEJ variations at different longitudes are due to the underlining effects of local winds, which are responsible for EEJ driving (Stening 1985, 1995). In addition, longitudinal differences in EEJ are caused by the different nature of the propagating diurnal tides, the meridional winds, and the dynamics of the migratory tides (Luhr et al. 2004; Rabiu et al. 2011). In this study, clear EEJ enhancement has been observed at the beginning of both the 2015 and 2018 storms. In the American region (Fig. 13e), EEJ resulted in VTEC variability in the initial phase, but no clear variability along the main phase. In the Asian region, the EEJ increment has been more prominent during the main phase (Fig. 13e`), leading to VTEC enhancements in the low-latitude stations (Fig. 4a-4c, 4a`-4c`). Our results demonstrate the existence of longitudinal variability due to EEJ during storm-time conditions. According to Lühr et al. (2004), dependencies of EEJ strength can be explained by varying the cross-section area of the longitudinal Cowling channel.

5. Conclusions

The upper atmospheric responses to 22-23 June 2015 and 25-26 August 2018 geomagnetic storms have been investigated for different regions of the world. The ionospheric variations during the storms are also showed in the context of different drivers at global and regional scales during the two storms. The main conclusions are as follows:

- Different regions have exhibited variable patterns of vTEC enhancements/depletions depending on thermospheric O/N2 ratio reduction/enrichment. In low latitude, the GNSS stations of East Asia (HYDE & IISC), South East Asia (COCO & BAKO), and Oceania (KOUC) have shown vTEC enhancement at the main phases of the storms. On the other side, the stations in South America (GLPS, KOUR and RIOP) registered no such enhancements. vTEC enhancement in the Asian and Oceania regions were approximately double the value as that during quite days. At the mid-latitudes of Oceania, East Asia, and Russia, the GNSS stations exhibited enhancements during both storms.
- The Swarm satellites vTEC confirmed the low-and mid-latitude ionospheric irregularities during main phase of both the storms.
- The GIM-TEC from IGS has also shown clear agreement with the GNSS-derived vTEC at most part of world during main phase of both the storms. These ionospheric variations at low-and mid-latitude regions during main phases of the both the storms are mainly driven by thermospheric O/N2 ratio, PPEF and EEJ.
- The PPEF variations at different longitudes provided different vTEC responses. These variations were clearly present in the low-and mid-latitude regions of Asia, Africa, Russia, and Oceania. The southward-northward oscillation of the IMF Bz component drives this variability along with interactions with Earth's Magnetosphere and solar wind. vTEC enhancements at different longitudes were mainly attributed to PPEF variability. vTEC depletions were mainly due to the enriched thermospheric winds composition, as seen by changes in the O/N_2 density ratio.
- The Dion from H-component of the Earth's magnetic field has exhibited clear variations during the 2015 storm as compared to 2018 storm. Moreover, significant EEJ is also noted in the low-latitude American and African stations during main phase of both the storms, that induced clear ionospheric variations.

Author Contributions

https://doi.org/10.5194/angeo-2022-18
Preprint. Discussion started: 5 September 2022

Annales Geophysicae Discussions

RS and MS did analysis and paper writing, MS designed the idea, AA, AH, AMM, NAN helped in paper revision, AH helped in the improvement of figures and paper writing, AC provided writing review and editing. M.A.H., I.K., A.M., E.A.A. reviewed the final draft. All authors have read and agreed to the published version of the manuscript.

Acknowledgments

The TIMED/GUVI data are available at https://guvitimed.jhuapl.edu/. The space weather indices are available at the NASA OMNI website http://omniweb.gsfc.nasa.gov/. The magnetometer data are available at https://www.intermagnet.org/. GNSS vTEC data of multiple stations is available at http://www.ionolab.org/. Swarm satellite data is available at https://vires.services/. Authors are appreciative of all the above sources for providing valuable datasets.

Conflicts of Interest

The authors declare no conflict of interest

References

Abdu, M. A., Maruyama, T., Batista, I. S., Saito, S., Nakamura, M., 2007. Ionospheric responses to the October 2003 superstorm: Longitude/local time effects over equatorial-low and mid-latitudes. Journal of Geophysical Research. 112:A10306. 10.1029/2006JA012228.

Adebesin, B. O., Ikubanni, S. O., Adebiyi, S.J., Joshua, B. W., 2013. Multi-station observation of ionospheric disturbance of March 9 2012 and comparison with IRI-model, Advances in Space Research. 52:604–613.

Adebiyi, S.J., Adeniyi, J.O., Adimula, I.A., Joshua, B., Gwani, M., 2012. Effect of the Geomagnetic Storm of April 5th to 7th, 2010, on the F2-Layer of the Ionosphere of Ilorin, Nigeria. World Journal of Engineering and Pure and Applied Science. 2(2):56–62.

Anderson, D., Anghel, A., Chau, J. L., Veliz, O., 2004. Daytime vertical E × B drift velocities inferred from ground-based magnetometer observations at low latitudes. Space Weather. 2:S11001. 10.1029/2004SW000095.

Araujo-Pradere, E. A., Fuller-Rowell, T. J., Spencer, P. S. J., 2006. Consistent features of the TEC changes during ionospheric storms. Journal of Atmospheric and Solar-Terrestrial Physics. 68(16):1834–1842. doi:10.1016/j.jastp.2006.06.

Arikan, F., Nayir, H., Sezen, U., Arikan, O., 2008. Estimation of single station interfrequency receiver bias using GPS-TEC. Radio Science. 43(4):1-13. 10.1029/2007RS003785.

Astafyeva, E., Zakharenkova, I., Alken, P., 2016. Prompt penetration electric fields and the extreme topside ionospheric response to the June 22–23, 2015 geomagnetic storm as seen by the Swarm constellation. Earth, Planets and Space. 152.

Astafyeva, E., Zakharenkova, I., Huba, J. D., Doornbos, E., Van den IJssel, J., 2017. Global ionospheric and thermospheric effects of the June 2015 geomagnetic disturbances: Multi-

https://doi.org/10.5194/angeo-2022-18
Preprint. Discussion started: 5 September 2022

Annales Geophysicae Discussions

instrumental observations and modeling. Journal of Geophysical Research: Space Physics. 122(11):716-742. https://doi.org/10.1002/2017JA024174.

Blanc, M., Richmond, A. D. 1980. The ionospheric disturbance dynamo. Journal of Geophysical Research. 85(A4):1669. https://doi.org/10.1029/ja085ia04p01669.

Binod, A., Dahal, S., and Chapagain, N. P. 2017. Study of field-aligned current (FAC), interplanetary electric field component (Ey), interplanetary magnetic field component (Bz), and northward (x) and eastward (y) components of geomagnetic field during supersubstorm, Earth and Space Science. 4:257–274. 10.1002/2017EA000258.

Buchert, S., Zangerl, F., Sust, M., André, M., Eriksson, A., Wahlund, J-E., Opgenoorth, H., 2015. SWARM observations of equatorial electron densities and topside GPS track losses. Geophysical Research Letters. 42:2088–2092. 10.1002/2015GL063121.

Buresova, D., Lastovicka, J., Hejda, P., Bochnicek, J., 2014. Ionospheric disturbances under low solar activity conditions. Advances in Space Research. 54(2):185-196. https://doi.org/10.1016/j.asr.2014.04.007.

Calabia, A., Jin, S., 2019. Supporting Information for "New modes and mechanisms of long-term ionospheric TEC variations from Global Ionosphere Maps". 10.1029/2019JA027703. Zenodo. https://doi.org/10.5281/zenodo.3563463

Calabia, A, Jin, S., 2020. New modes and mechanisms of long-term ionospheric TEC variations from Global Ionosphere Maps", Journal of Geophysical Research. Space Physics. 125(6). 10.1029/2019JA027703.

Calabia, A, C Anoruo, S Munawar, C Amory-Mazaudier, Y Yasyukevich, C Owolabi, and S Jin (2022). Low-Latitude Ionospheric Responses and Coupling to the February 2014 Multiphase Geomagnetic Storm from GNSS, Magnetometers, and Space Weather Data, Atmosphere, 13, 518. doi:10.3390/atmos13040518.

Chartier, A. T., Mitchell, C. N., Miller, E. S., 2018. Annual occurrence rates of ionospheric polar cap patches observed using Swarm. Journal of Geophysical Research: Space Physics. 123:2327–2335. https://doi.org/10.1002/2017JA024811.

Christensen, A. B., et al. (2003), Initial observations with the Global Ultraviolet Imager (GUVI) in the NASA TIMED satellite mission, J. Geophys. Res., 108(A12), 1451, doi:10.1029/2003JA009918.

Cole, K. D., 1966. Magnetic storms and associated phenomena. Space Science Reviews. 5:699–770.

Fang, H., Weng, L., Sheng, Z., 2012. Variations in the thermosphere and ionosphere response to the 17–20 April 2002 geomagnetic storms. Advances in Space Research. 49:1529–1536.

Fagundes, P. R., Cardoso, F. A., Fejer, B. G., Venkatesh, K., Ribeiro, B. A. G., Pillat, V. G., 2016. Positive and negative GPS-TEC ionospheric storm effects during the extreme space weather event of March 2015 over the Brazilian sector. Journal of Geophysical Research: Space Physics. 121:5613–5625. 10.1002/2015JA022214.

Fejer, B. G., Jensen, J. W., Su, S., 2008. Quiet time equatorial F region vertical plasma drift model derived from ROCSAT-1 observations. Journal of Geophysical Research: Space Physics. 113:A5. https://doi.org/10.1029/2007JA012801.

Fuller-Rowell,T.J., Codrescu, M. V., Moffelt, R.J., Quegan. S., 1994. Response of thermosphere and ionosphere to geomagnetic storms. Journal of Geophysical Research. 99:3893-391.

Fuller-Rowell, T. J., Millward, G. H., Richmond, A. D., Codrescu, M. V., 2002. Storm-time changes in the upper atmosphere at low latitudes. Journal of Atmospheric and Solar-Terrestrial Physics. 64(12–14):1383–1391. https://doi.org/10.1016/s1364-6826(02)001013.

https://doi.org/10.5194/angeo-2022-18
Preprint. Discussion started: 5 September 2022

Annales Geophysicae Discussions

Fuller-Rowell, T. J., 2011. Storm-time response of the thermosphere-ionosphere system. Aeronomy of the Earth's Atmosphere and Ionosphere. 2:419–435). https://doi.org/10.1007/978-94-007-0326-1.

Gao, Q., Liu, L., Zhao, B., Wan, W., Zhang, M., Ning, B., 2008. Statistical study of the storm effects in middle and low latitude ionosphere in the East-Asian sector, Chinese Journal of Geophysics. 51:435–443.

Hargreaves, J. K., 1992. The Solar-Terrestrial Environment. Cambridge University Press. https://doi.org/10.1017/CBO9780511628924.

Heelis, R. A., 2004. Electrodynamics in the low and middle latitude ionosphere. Journal of Atmospheric and Solar - Terrestrial Physics. 66(10):825–838. https://doi.org/10.1016/j.jastp.2004.01.034.

Hernández-Pajares, M., Juan, J., Sanz, J., 1999. New approaches in global ionospheric determination using ground GPS data. Journal of Atmospheric and Solar-Terrestrial Physics. 61(16):1237–1247. 0.1016/S1364-6826(99)00054-1.

Huang, C. S., Foster., J. C., Kelley, M. C., 2005. Long-durationpenetration of the interplanetary electric field to the low-latitudeionosphere during the main phase of magnetic storms. Journal of Geophysical Research. 110:A11309

Jaggi, R. K., Wolf, R. A., 1973. Self-consistent calculation of the motion of a sheet of ions in the magnetosphere. Journal of Geophysical Research. 78:2852.

Joshua, B., Adeniyi, J.O., Adimula, I. A., Abbas, M., Adebiyi, S.J., 2011. The Effect of Magnetic Storm of May 2010 on the F2 Layer over the Ilorin Ionosphere. World Journal Young Researchers. 1(5):71–78.

Kashcheyev, A., Migoya-Orué, Y., Amory-Mazaudier, C., Fleury, R., Nava, B., Alazo-Cuartas, K., Radicella, S. M., 2018. Multivariable Comprehensive Analysis of Two Great Geomagnetic Storms of 2015. Journal of Geophysical Research: Space Physics. 123(6):5000–5018. https://doi.org/10.1029/2017ja024900.

Kassa, T., Damtie, B., 2017.Ionospheric irregularities over Bahir Dar, Ethiopia during selected geomagnetic storms. Advances in Space Research. 60(1):121-129. https://doi.org/10.1016/j.asr.2017.03.036.

Kelley, M. C., Fejer, B. G., Gonzales, C. A., 1979. An explanation foranomalous ionospheric electric fields associated with a northwardturning of the interplanetary magnetic field. Geophysical Research Letters. 6:301–304.

Klimenko, M.V., Klimenko, V.V., Ratovsky, K.G., Goncharenko, L.P.,2011. Disturbances in the ionospheric F-region peak heights in the American longitudinal sector during geomagnetic storms of September 2005, Advances in Space Research. 48(7):1184-1195. https://doi.org/10.1016/j.asr.2011.06.002.

Klobuchar, J. A., 1987. Ionospheric Time-Delay Algorithm for Single-Frequency GPS Users. IEEE Transactions on Aerospace and Electronic Systems. AES-23(3):325–31. 10.1109/TAES.1987.310829.

Kikuchi, T., Lühr, H., Schlegel, K., Tachihara, H., Shinohara, M., Kitamura, T.-I., 2000. Penetration of auroral electric fields to the equator during a substorm. Journal of Geophysical Research: Space Physics. 105(A10):23251–23261. https://doi.org/10.1029/2000ja900016.

Le H., Amory-Mazaudier, C., 2005. Magnetic signature of the ionospheric disturbance dynamo at equatorial latitudes: "Ddyn." Journal of Geophysical Research. 110(A10). https://doi.org/10.1029/2004ja010578.

https://doi.org/10.5194/angeo-2022-18
Preprint. Discussion started: 5 September 2022

Lissa, D., Srinivasu, V. K. D., Prasad, D. S. V. V. D., Niranjan, K., 2020. Ionospheric response to the 26 August 2018 geomagnetic storm using GPS-TEC observations along 80° E and 120° E longitudes in the Asian sector. Advances in Space Research. 66:1427-1440.
Lu. G., 2006. High-Speed Streams, Coronal Mass Ejections, and Interplanetary Shocks: A Comparative Study of Geoeffectiveness. Recurrent Magnetic Storms: Corotating Solar Wind Streams. 167. https://doi.org/10.1029/167GM10.
Luhr, H., Maus, S., Rother, M., 2004. Noon-time equatorial electrojet: Its spatial features as determined by the CHAMP satellite. Journal of Geophysical Research. 109:A01306. 10.1029/2002JA009656.
Mannucci, A.J., Tsurutani, B.T., Iijima, B.A., Saito, A., Gonzalez, W.D., Guarnieri, F.L., Kozyra, J.U., Skoug, R., 2005. Dayside global ionospheric response to the major interplanetary events of October 29–30, 2003 ‘‘Halloween Storms’’. Geophysical Research Letters. 32:L12S02. 10.1029/2004GL021467.
Mannucci, A.J., Tsurutani, B.T., Abdu, M.A., Gonzalez, W.D., Komjathy, A., Echer, E., Iijima, B.A., Crowley, G., Anderson, D., 2008. Superposed epoch analysis of the dayside ionospheric response to four intense geomagnetic storms. Journal of Geophysical Research. 113:A00A02. 10.1029/2007JA012732.
Martinis, C. R., Mendillo, M. J., and Aarons, J., 2005. Toward a synthesis of equatorial spread F onset and suppression during geomagnetic storms. Journal of Geophysical Research. 110(A07306). 10.1029/2003JA010362.
Mene, N. M., Kobéa, A. T., Obrou, O. K., Zaka, K. Z., Boka, K., Amory-Mazaudier C., Assamoi. P., 2011. Statistical study of the DP2 enhancement at the dayside dip-equator compared to low latitudes. Annales Geophysicae. 2225-2233.
Mayaud, P. N., 1965. Analyse morphologique de la variabilité jour-à-jour de la variation journalière régulière SR du champ magnétique terrestre, I- le système de courants Cp (régions polaires et subpolaires). Annales Geophysicae. 21:369–401.
Nishida, A., 1968. Coherence of geomagnetic DP2 fluctuationswith interplanetary magnetic variations. Journal of Geophysical Research. 73:5549–5559.
Prölss, G.W., and M. K. Bird (2010), "Physics of the Earth's Space Environment", Springer Verlag, Heidelberg.
Rabiu, A. B., Yumoto, K., Falayi, E. O., Bello, O. R., MAGDAS/CPMN Group., 2011. Ionosphere over Africa: Results from geomagnetic field measurement during international Heliophysical Year IHY. Journal of Sun and Geosphere. 6:61–64.
Roma-Dollase, D., Hernández-Pajares, M., Krankowski, A., Kotulak, K., Ghoddousi-Fard, R., Yuan, Y., Li, Z., Zhang, H., Shi, C., Wang, C., Feltens, J., Vergados, P., Komjathy, A., Schaer, S., García-Rigo, A., Gómez-Cama, J. M., 2018 .Consistency of seven different GNSS global ionospheric mapping techniques during one solar cycle. Journal of Geodesy. 92(6):691–706. https://doi.org/10.1007/s00190-017-1088-9.
Shah, M., Calabia, A. G., Tariq, M. A., Ahmed, J., Ahmed, A., 2020. Possible ionosphere and atmosphere precursory analysis related to Mw > 6.0 earthquakes in Japan. Remote Sensing of Environment. 239:111620. https://doi.org/10.1016/j.rse.2019.111620.
Sharma, S., P. Galav, N., Dashora, S., Alex, R. S., Dabas, R., Pandey. 2011. Response of low-latitude ionospheric total electron content to the geomagnetic storm of 24 August 2005. Journal of Geophysical Research. 116:A05317. 10.1029/2010JA016368.
Shao, X., Guzdar, P. N., Milikh, G. M., Papadopoulos, K., Goodrich, C. C., Sharma, A., Wiltberger, M. J., Lyon, J. G., 2002. Comparing ground magnetic field perturbations from

https://doi.org/10.5194/angeo-2022-18
Preprint. Discussion started: 5 September 2022

global MHD simulations with magnetometer data for the 10 January 1997 magnetic storm event. Journal of Geophysical Research: Earth Surface. 107.
Stankov, S.M., Jakowski, N., 2007. Ionospheric effects on GNSS reference network integrity. Journal of Atmospheric and Solar-Terrestrial Physics. 69(4–5):485–499. 10.1016/j.jastp.2006.08.008.
Stankov, S.M., Warnant, R., Stegen, K., 2009. Trans-ionospheric GPS signal delay gradients observed over mid-latitude Europe during the geomagnetic storms of October–November 2003. Advances in Space Research. 43(9):1314–1324. 10.1016/j.asr.2008.12.012.
Stankov, S.M., Stegen, K., Warnant, R., 2010. Seasonal variations of storm-time TEC at European middle latitudes. Advances in Space Research. 48:1318–1325.
Stening, R. J., 1985. Modeling the equatorial electrojet, Journal of Geophysical Research. 90:1705–1719. 10.1029/JA090iA02p01705.
Stening, R. J., 1995. Variations in the strength of the Sq current system. Annals of Geophysics. 13:627–632.
Tsurutani, B. T., Mannucci, A. J., Iijima, B. A., Sobral, J. H., Gonzalez, W. D., Gaurnieri, F. L., Tsuda, T., Saito, A., Yumoto, K., Fejer, B., Fuller-Rowell, T., Kozyra, J. U., Foster, J. C., Coster, A. J., Vasyliuas, V. M., 2004. Global dayside ionospheric uplift and enhancement associated with interplanetary electric fields. Journal of Geophysical Research. 109:A08302.
Vankadara, R. K., Panda, S. K., Amory-Mazaudier, C., Fleury, R., Devanaboyina, V. R., Pant, T. K., Jamjareegulgarn, P., Haq, M. A., Okoh, D., Seemala, G. K., 2022. Signatures of Equatorial Plasma Bubbles and Ionospheric Scintillations from Magnetometer and GNSS Observations in the Indian Longitudes during the Space Weather Events of Early September 2017. Remote Sensing. 14:652. https://doi.org/10.3390/rs14030652.
Warnant, R., Lejeune, S., Bavier, M., 2007. Space Weather influence on satellite based navigation and precise positioning. Space Weather – Research towards Applications in Europe. 129–146.
Wei, Y., Pu, Z., Hong, M., 2010. Long-lasting goodshielding at the equatorial ionosphere. Geophysical Research Letters. 115:A12256.
Xiong, C., Stolle, C., Luhr, H., Park, J., Fejer, B. G., Kervalishvili, G. N., 2016a. Scale analysis of equatorial plasma irregularities derived from Swarm constellation. Earth, Planets and Space. 68(1). https://doi.org/10.1186/s40623-016-0502-5.
Yamazaki, Y., Kosch, M. J., 2015. The equatorial electrojet during geomagnetic storms and substorms. Journal of Geophysical Research: Space Physics. 120(3). 10.1002/2014JA020773.
Zaourar, N., Amory-Mazaudier, C., Fleury, R., 2017. Hemispheric asymmetries in the ionosphere response observed during the high-speed solar wind streams of the 24–28 August 2010. Advances in Space Research. 59(9):2229–2247. https://doi.org/10.1016/j.asr.2017.01.04.